TOWARDS IMPROVED TIME-SERIES INSAR ANALYSIS WITH A MULTI-DEPTH MULTI-FOCUSING TIME-DOMAIN BACKPROJECTION SAR ALGORITHM

Stacey A. Huang

NASA Postdoctoral Program Fellow
Geodesy and Geophysics Laboratory
NASA Goddard Space Flight Center

Ettore Biondi

Seismological Laboratory
Div. of Geological and Planetary Sciences
California Institute of Technology

ABSTRACT

SAR imagery is traditionally produced in range-Doppler geometry. While such algorithms are computationally efficient, they require multiple assumptions regarding signal properties. Time-domain backprojection (TDBP) SAR focusing methods require fewer assumptions and are considerably more robust to perturbations in flight paths and target geometry. Furthermore, TDBP produces single-look complex (SLC) imagery that is directly geocoded, which simplifies subsequent analysis compared to range-Doppler products. With modern improvements in computational power, TDBP SAR-focusing methods have become viable alternatives to range-Doppler. However, TDBP-formed imagery can be sensitive to inaccuracies in global DEMs. Here, we investigate the so-called multi-depth multi-focusing algorithm that has been proposed to correct for DEM errors. We analyze changes in the detection of persistent scatterers (PS) and find that while *depth-averaged* SLCs yield fewer PS, *depth-optimized* SLCs yield more PS and produce higher-quality interferograms compared with unoptimized SLCs. We conclude by discussing the implications for improved time-series InSAR analysis.

Index Terms— interferometric synthetic aperture radar (InSAR), persistent scatterers, digital elevation models (DEMs)

1. INTRODUCTION

Time-domain backprojection (TDBP) algorithms are a robust alternative to traditional frequency-domain methods for focusing SAR imagery. While traditionally viewed as computationally intensive, TDBP methods are straightforward to implement — they only require accurate knowledge of both the flight/orbital path of the imaging aircraft or spacecraft and an estimate of the target location, usually given by a digital elevation model (DEM) [1]. Because TDBP methods solve explicitly for complex flight or orbital geometry, they are highly resistant to unknown perturbations and also produce images directly in regularly gridded map coordinates [2, 3]. Recent advances — in particular, the accuracy of modern flight and orbit trackers and recent advances in computing such as GPU-accelerated parallelization [4–7] — have virtually eliminated conventional barriers to implementing TDBP methods. As a result, TDBP methods have gained traction for use in differential interferometric SAR (DInSAR) and time-series InSAR applications with the introduction of geocoded SLCs, which reduce storage requirements and vastly simplify interferogram formation for end-users [8, 9]. Previous work has also shown that the density of persistent scatterers (PS) increases when SLCs are directly geocoded to map geometry due to more accurate interferogram coregistration [10].

One drawback of TDBP methods is the requirement for fairly accurate estimates of source and receiver geometry. A DEM error of 10 m, which is common in widely used global DEMs for InSAR processing [11], results in a 4 mm error in deformation estimates [12]. This measurement accuracy can be insufficiently sensitive when fine deformation estimates are required, including for studies of moderate fault creep and coastal subsidence. Furthermore, a 10-m DEM error may result in a drop in SNR when targets are offset from the assumed scattering cell center, resulting in suboptimal focusing [1].

The so-called multi-depth multi-focusing technique has previously been proposed as a possible method to correct for positioning errors in TDBP SAR imagery [13]. Because TDBP focuses radar returns directly in geodetic coordinates given known positions of the source (from orbit information) and targets (from a DEM), the focusing "depth" (i.e., the line-of-sight distance from the source to the target) can be easily adjusted during the image formation procedure. Thus, the multi-depth multi-focusing algorithm proposed to form a set of depth-offset SLCs per single SLC by varying the focusing depth relative to the DEM, then averaging all depth-offset slices to form a *depth-averaged* SLC. The possibility of forming a *depth-optimized* SLC, where each SLC is focused to the depth that maximizes the observed signal-to-noise ratio (SNR), was also raised but not further investigated. Preliminary results showed that the depth-averaged SLC improved the observed SNR, with a speckle-reducing effect similar to multi-looking without a loss in spatial resolution. Fig. 1 shows an example of the improvement in SNR for a multi-focused SLC over a depth range of -20 to 20 m using ALOS-1 (L-band) data over Cambodia [13].

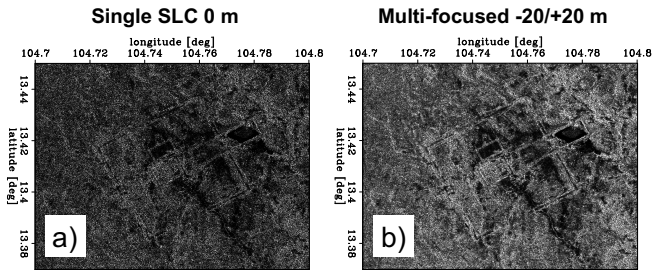

Fig. 1. The ruins of a temple complex in the heavily forested Prasat Bakan in Cambodia for a) an unoptimized SLC and b) a multi-focused (depth-averaged) SLC from -20 to 20 m using ALOS-1 data, reproduced from [13]. The SNR of the depth-averaged SLC is clearly much higher.

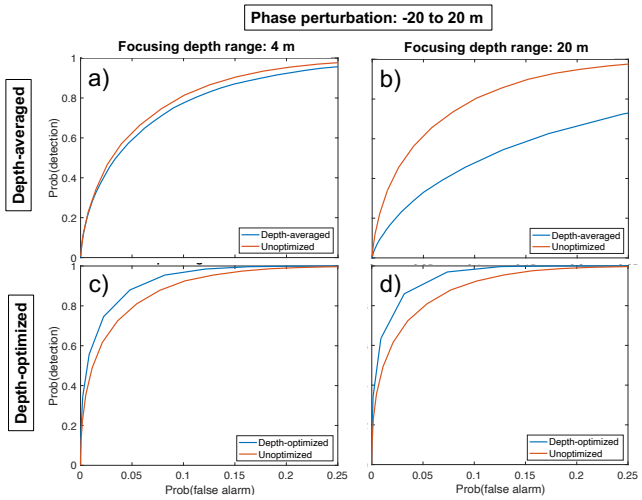

Fig. 2. Receiver operating characteristic (ROC) curves of true PS detection for depth-averaged SLCs (a and b) and depth-optimized SLCs (c and d) for different focusing depth ranges. A deeper focusing depth range decreases PS detection in the depth-averaging case but improves PS detection in the depth-optimized case.

Here, we extend previous work by analyzing the applicability of depth-averaged and depth-optimized SLCs for time-series PS-InSAR analysis.

2. METHODOLOGY AND DATA

A simple model suffices to demonstrate the multi-depth effect. Suppose we have $i = 1, ..., N$ (non-deforming) scenes. Then each scene s_i can be described as the sum of a real correlated component c and a noise component n_i [14, 15]:

$$s_i = c + n_i = a_i e^{j\frac{4\pi}{\lambda}\phi_i} \tag{1}$$

where the alternate phasor notation is also presented, with amplitude a_i, phase ϕ_i, and imaging wavelength λ. In this work, we assumed that c is exponentially distributed in power with a mean of 1/2 and that n_i is a circularly symmetric Gaussian. We then added a phase noise term ϕ_n, such that

$$s_i = a_i e^{j\frac{4\pi}{\lambda}(\phi_i+\phi_n)}. \tag{2}$$

For simplicity, we introduced ϕ_n as a spatial linear ramp across all pixels in our simulations, using a range of -20 to 20 m over 100,000 pixels. Then, to compute the depth-averaged SLC, we formed s_i such that

$$s_i = \sum_k a_i e^{j\frac{4\pi}{\lambda}(\phi_i+\phi_n+d_k)} \tag{3}$$

where d_k are the depth offsets. We formed uniformly spaced SLCs with a step size of 2 m and depth ranges of 4 and 20 m. To compute the depth-optimized SLC, we used a linear global search with the same step size and depth ranges as the depth-averaged case but instead formed s_i such that

$$s_i = a_i e^{j\frac{4\pi}{\lambda}(\phi_i+\phi_n+d_{opt})} \tag{4}$$

where d_{opt} was chosen as the value of d that maximized the signal-to-clutter ratio (SCR, γ) as estimated using the parametric phase-based maximum likelihood (MLE) PS detector using Gaussian scattering assumptions [16]:

$$\begin{aligned} d_{opt} &= \arg\max_d \gamma_{est} \\ &= \arg\max_d [\arg\max_\gamma f(\gamma|\phi_{n1}+d, \cdots \phi_{nN}+d)]. \end{aligned} \tag{5}$$

When applied to real data, the SLCs should be focused using a traditional TDBP method (e.g., as described in Zebker [9]) with the depth offsets d_k or d_{opt} included as an additive phase term during SLC resampling to the DEM. Specifically, the focused signal for each resolution element can be expressed as the sum of the signal from all contributing scatterers, D_n, where $n \in \mathcal{N}$, corrected by the propagation phase ϕ_{prop}, which is given by the difference of the distance from the zero-Doppler source point $s_0(x, y, z)$ to the target position $p(x', y', z')$ and perturbed by the depth offset d:

$$s_i = \sum_{n\in\mathcal{N}} D_n e^{j\frac{4\pi}{\lambda}|s_0(x,y,z)-p(x',y',z')+d|} \tag{6}$$

For this study, we examined TDBP-focused Sentinel-1 imagery over select areas on the islands of Kilauea, Hawai'i and Tutuila, American Samoa from 2015-2022. Both islands are volcanic, though Tutuila is smaller, more vegetated, and overall less temporally coherent compared with Kilauea. We formed unoptimized SLCs at native resolution that were geocoded using NASADEM, then formed depth-averaged and depth-optimized SLCs. We implemented a parallelized GPU-accelerated workflow to minimize the increase in com-

Table 1. PS Density (count/km^2) for depth-averaged ("Avg.") and depth-optimized ("Opt.") SLCs

	Kilauea		Tutuila	
Focus Rng.	Avg.	Opt.	Avg.	Opt.
0 m (None)	352.07	352.07	4.23	4.23
4 m	298.74	532.65	2.71	8.18
20 m	272.30	606.25	2.49	26.32

putational load. To identify PS, we used the Maximum Likelihood PS detector with a parametric Gaussian model [16]. We repaired decorrelated portions of the interferograms with the phase similarity PS interpolation algorithm using the standard 20-pixel search window [17].

3. RESULTS AND DISCUSSION

Our simulations predicted a decrease in the rate of PS detection with depth-averaged SLCs and an improvement in the rate of PS detection with depth-optimized SLCs, with a greater difference with a larger focusing depth range. Fig. 2 shows the receiving operating characteristic (ROC) curves for depth-averaged and depth-optimized SLCs.

Our data were consistent with these predictions. Table 1 shows the comparison of PS density for averaged vs. depth-optimized SLCs over both Kilauea and Tutuila Islands. In both areas, depth-averaged SLCs yielded fewer PS, especially for a larger focusing range. By contrast, depth-optimized SLCs yielded significantly more PS. In Kialuea, the 20 m depth-optimized SLC yielded roughly 2x the PS density compared to the unoptimized version, and in Tutuila, the 20 m depth-optimized SLC yielded more than 6x the density.

Figs. 3 and 4 show the original, PS-interpolated, depth-optimized, and both PS-interpolated and depth-optimized interferograms for Kilauea and Tutuila. The depth-optimized algorithm drastically improves the interferogram quality and is able to fill decorrelated gaps in both areas, which in turn significantly enhances PS-interpolated interferograms compared to the original.

4. CONCLUSIONS AND FUTURE WORK

Our study demonstrates the promise of using depth-optimized SLCs for improving interferogram quality over two diverse terrain types. We obtained good results even using a simple global search method. Our observations from simulated and real data demonstrated that our algorithm results in up to a 6x densification of PS, with improvements primarily observed in mid-to-high correlation regions.

Future work will compare the quality of time-series results derived from PS-InSAR using depth-optimized SLCs compared with unoptimized SLCs. We will also analyze changes in the quality of multilooked interferograms that can be used in small baseline subset (SBAS) time-series methods. Further studies are also needed to understand the relationship of the technique with elevation correction and to investigate opportunities for integration with 3D focusing methods such as tomographic SAR [18, 19]. We have observed in preliminary tests that using depth-optimized SLCs reduces variations in the derived time-series results from different DEMs (e.g., the NASADEM and Copernicus products), but further work is needed to understand these results.

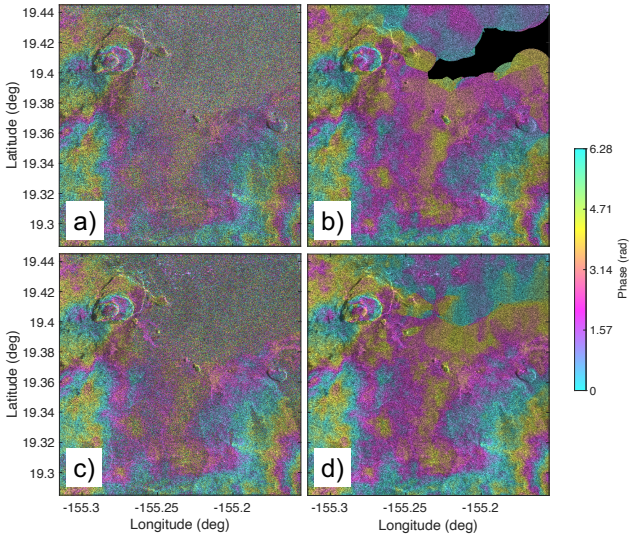

Fig. 3. Detail over Kilauea of four variants of the same interferogram formed between scenes acquired on October 29, 2018, and November 10, 2018. a) Original, uninterpolated, unoptimized interferogram. b) Unoptimized interferogram with PS interpolation following Wang and Chen [17], where decorrelated regions are masked out in black. c) Uninterpolated, depth-optimized interferogram. d) Depth-optimized and PS-interpolated interferogram. Both interferogram quality and PS interpolation are significantly improved with depth-optimized SLCs.

Overall, depth-optimized SLCs exhibit a strong potential to improve the quality of deformation measurements that can be produced using easily accessible global DEMs from TDBP InSAR time-series analysis, which will play a critical role in expanding the accessibility of powerful user-friendly tools for imaging subtle geophysical phenomena around the globe.

5. ACKNOWLEDGEMENTS

S. A. Huang is supported by the NASA Postdoctoral Program at the NASA Goddard Space Flight Center, administered by the Oak Ridge Associated Univerities (ORAU) under contract with NASA. Copernicus Sentinel data 2015-2022 were provided by ASF DAAC, accessed from Janurary to April 2023 from https://asf.alaska.edu.

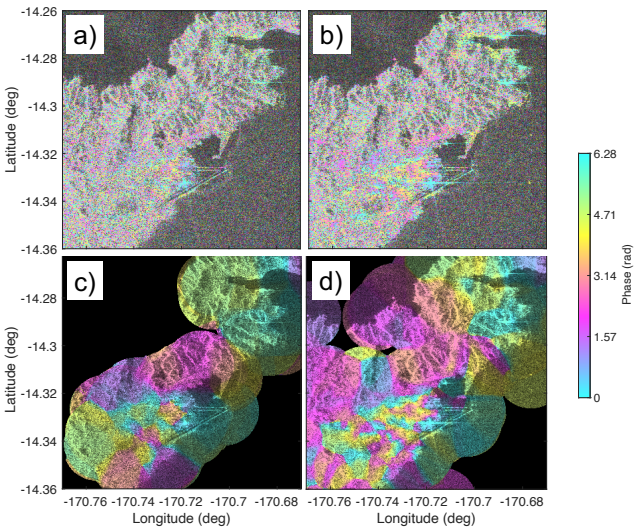

Fig. 4. Same as Fig. 3, but over Tutuila, with four variants of the interferogram formed between the scenes acquired on October 24, 2018, and November 5, 2018. a) Original unimproved and uninterpolated interferogram. b) Original and unoptimized but PS-interpolated interferogram. c) Depth-optimized but uninterpolated interferogram. d) Depth-optimized and PS-interpolated interferogram. The depth-optimized SLC significantly improves the quality of the interferogram, even in challenging terrain.

6. REFERENCES

[1] M. I. Duersch, *Backprojection for Synthetic Aperture Radar*, Ph.D. thesis, Brigham Young University, 2013.

[2] P. Prats, A. Reigber, and J. Mallorqui, "Topography-Dependent Motion Compensation for Repeat-Pass Interferometric SAR Systems," *IEEE Geosci. Remote Sens. Lett.*, vol. 2, no. 2, pp. 206–210, apr 2005.

[3] L. J. Harcke, "Time-domain backprojection for precise geodetic coding of spaceborne SAR imagery," in *IEEE Natl. Radar Conf.*, 2009, pp. 27–29.

[4] H. A. Zebker, S. Hensley, P. Shanker, and C. Wortham, "Geodetically accurate InSAR data processor," *IEEE Trans. Geosci. Remote. Sens.*, vol. 48, no. 12, pp. 4309–4321, 2010.

[5] A. Fasih and T. Hartley, "GPU-accelerated synthetic aperture radar backprojection in CUDA," in *IEEE Natl. Radar Conf.*, 2010, pp. 1408–1413.

[6] O. Frey, C. L. Werner, and U. Wegmuller, "GPU-based parallelized time-domain back-projection processing for Agile SAR platforms," in *IEEE IGARSS 2014*, 2014, pp. 1132–1135.

[7] A. Capozzoli, C. Curcio, and A. Liseno, "FAST GPU-BASED INTERPOLATION FOR SAR BACK-PROJECTION," *Prog. Electromagn. Res.*, vol. 133, no. September, pp. 259–283, 2013.

[8] Y. Zheng and H. A. Zebker, "Phase correction of single-look complex radar images for user-friendly efficient interferogram formation," *IEEE J. Sel. Top. Appl. Earth Obs. Remote Sens.*, vol. 10, no. 6, pp. 2694–2701, 2017.

[9] H. A. Zebker, "User-Friendly InSAR Data Products: Fast and Simple Timeseries Processing," *IEEE Geosci. Remote Sens. Lett.*, vol. 14, no. 11, pp. 2122–2126, 2017.

[10] C. Magnard, U. Wegmüller, and C. Werner, "Persistent scatterer interferometry in mountainous areas: Advantages of working in map geometry," *Procedia Comput. Sci.*, vol. 181, no. 2020, pp. 198–205, 2021.

[11] E. Uuemaa, S. Ahi, B. Montibeller, M. Muru, and A. Kmoch, "Vertical accuracy of freely available global digital elevation models (aster, aw3d30, merit, tandem-x, srtm, and nasadem)," *Remote Sensing*, vol. 12, no. 21, pp. 3482, 2020.

[12] H. A. Zebker, "Answers to Questions about User-Friendly Insar Data Products," in *IEEE IGARSS 2019*, 2019, pp. 354–356.

[13] E. Biondi, S. H. Yun, J. Jung, H. A. Zebker, and R. J. Michaelides, "Multi-depth multi-focusing SAR algorithm," in *AGU Fall Meeting 2020*, 2020.

[14] P. S. Agram, *Persistent Scatterer Interferometry in Natural Terrain*, Ph.D. thesis, Stanford University, 2010.

[15] S. A. Huang, *Statistical Theory for the Detection of Persistent Scatterers in InSAR Imagery*, Ph.D. thesis, Stanford University, 2021.

[16] P. S. Agram and H. Zebker, "Persistent scatterer selection using maximum likelihood estimation," *Geophys. Res. Lett.*, vol. 34, no. 22, pp. L22301, 2007.

[17] K. Wang and J. Chen, "Accurate Persistent Scatterer Identification Based on Phase Similarity of Radar Pixels," *IEEE Trans. Geosci. Remote. Sens.*, vol. 60, pp. 1–13, 2022.

[18] X. X. Zhu and R. Bamler, "Very High Resolution Spaceborne SAR Tomography in Urban Environment," *IEEE Trans. Geosci. Remote. Sens.*, vol. 48, no. 12, pp. 4296–4308, 12 2010.

[19] G. Fornaro, F. Lombardini, A. Pauciullo, D. Reale, and F. Viviani, "Tomographic processing of interferometric SAR data: Developments, applications, and future research perspectives," *IEEE Signal Process. Mag.*, vol. 31, no. 4, pp. 41–50, 2014.